AGU PUBLICATIONS

JGR

Journal of Geophysical Research: Earth Surface

RESEARCH ARTICLE

10.1002/2013JF003064

Key Points:
- An approximate model for the flow field on intertidal platforms is discussed
- Influence of advection on sediment dynamics is negligible for vegetated platform
- The model is a suitable tool for long-term morphodynamic models

Correspondence to:
T. Van Oyen,
tomas.vanoyen@ugent.be

Citation:
Van Oyen, T., L. Carniello, A. D'Alpaos, S. Temmerman, P. Troch, and S. Lanzoni (2014), An approximate solution to the flow field on vegetated intertidal platforms: Applicability and limitations, *J. Geophys. Res. Earth Surf.*, *119*, doi:10.1002/2013JF003064.

Received 11 DEC 2013
Accepted 8 JUL 2014
Accepted article online 12 JUL 2014

An approximate solution to the flow field on vegetated intertidal platforms: Applicability and limitations

T. Van Oyen[1,2], L. Carniello[3], A. D'Alpaos[4], S. Temmerman[5], P. Troch[1], and S. Lanzoni[2]

[1]Department of Civil Engineering, Ghent University, Ghent, Belgium, [2]Flanders Hydraulics Research, Antwerp, Belgium, [3]Department of Civil, Architectural and Environmental Engineering, University of Padua, Padua, Italy, [4]Department of Geosciences, University of Padua, Padua, Italy, [5]Ecosystem Management Research Group, University of Antwerp, Antwerp, Belgium

Abstract Tidal wetland evolution is governed by interactions between topography, vegetation, and the flow field. Aiming to provide an appropriate hydrodynamic tool within a long-term geomorphic model of vegetated wetlands, we describe an approximate procedure to model the depth-averaged flow field on vegetated intertidal platforms. The procedure is tested by a qualitative comparison with laboratory experiments and quantitatively comparing with a numerical model, focusing on the influence of spatial variations in friction on the flow field. Overall, satisfactory comparisons are obtained. Nevertheless, some limitations of the approach are apparent. These are discussed in the light of the model assumptions. We analyze the impact of the observed limitations on the ability of the approximate solution to describe the morphodynamic evolution of the bed elevation. This is performed by evaluating the changes in the bed elevation after one tidal cycle on the intertidal platform based on flow velocities obtained with a numerical model and those of the simplified procedure. It is found that the bed evolution on the platform is reasonably described with the approximate solution, even though the accumulation of sediment is underestimated near the watershed divide by the approximate model. Taking into account the computationally economic character of the approximate procedure, the analysis indicates that the model provides a suitable tool to investigate the long-term morphodynamic evolution of tidal wetlands.

1. Introduction

1.1. Context

Salt marshes and mangrove forests are common features of lagoonal and estuarine environments. These geomorphological landscapes are characterized by vegetated intertidal platforms which are periodically flooded by the tide and are dissected by a network of branching and meandering channels. Hosting a diversity of habitat-specific species, acting as an organic carbon sink and providing a significant part of the primary production in the coastal zone [*Mitsch*, 2000], salt marshes and mangrove forests contain substantial ecological and economic value [*Costanza et al.*, 1997].

Presently, the existence of these wetlands is challenged by climatic changes such as sea level rise and global warming, and by anthropogenic influences [e.g., disturbances in sediment supply, *Day et al.*, 2000]. The possible submergence and die-off of vegetation cover leads to fundamental questions such as the following: (1) Are salt marshes and mangrove forests able to keep up with current and predicted rates of sea-level rise? and (2) What will be the morphodynamic planimetric evolution of these intertidal features?

Over the past decades, several point [e.g., *Allen*, 1990; *French*, 1993; *Morris et al.*, 2002; *D'Alpaos et al.*, 2011], one-dimensional [*Tambroni and Seminara*, 2012] and two-dimensional [e.g., *D'Alpaos et al.*, 2007; *Kirwan and Murray*, 2007] models have been developed to study the evolution of intertidal marshes. The results of these models illustrate that the overall evolution of tidal wetlands is controlled by interactions between vegetation cover, platform topography, and the flow field.

A common characteristic of these studies (especially of the two-dimensional models) is the introduction of simplified approaches. This is motivated by the objective to investigate a phenomenon evolving over long time scales ($\sim\mathcal{O}$(100 years)) and on a large spatial area ($\sim\mathcal{O}(10^3)$ ha). In particular, the models adopted in these studies aim to reliably describe the key processes, while limiting the computational cost, in order to facilitate the understanding of the essential feedbacks which control the dynamical evolution of vegetated tidal wetlands. It is within this context that there is still a need for simplified hydrodynamical models, see *Fagherazzi et al.* [2012] for a recent overview.

Figure 1. The occurrence of vegetation patches on an intertidal platform in the Westerscheldt (Hooge Springer), The Netherlands. Figure adopted from *Balke et al.* [2012].

1.2. Simplified Approaches to Describe Frictionally Dominated Tidal Flows

One of the most popular simplified models currently used to evaluate the flow field on an intertidal platform is that proposed by *Rinaldo et al.* [1999]. This model was introduced in order to automatically identify the watersheds on shallow tidal areas and to evaluate the relationships between geometric properties of tidal channel networks and their corresponding contributing area [*Rinaldo et al.*, 1999; *Marani et al.*, 2003; *D'Alpaos et al.*, 2005]. The simplified approach embodied by the model relies on the observation that in micro tidal environments the flow field on the intertidal platforms, due to the typically shallow depth and the possible presence of a vegetation cover, is dominated by friction.

LeBlond [1978] was the first to adopt a simplified approach to describe a tidal flow field dominated by friction. Using a scaling analysis, *LeBlond* [1978] showed that tidal propagation in shallow tidal rivers is characterized by frictional forces which exceed the inertial acceleration during most of the tidal cycle. Combining momentum and mass conservation equations, *LeBlond* [1978] obtained a nonlinear diffusion equation for the tidal velocity. Further simplifying the problem by assuming a constant diffusion coefficient, *LeBlond* [1978] provided a simple explanation to the large time lags between the free surface elevation at a river mouth and the upstream sections for very low tides.

The zero inertia approximation introduced by *LeBlond* [1978] was subsequently applied by *Friedrichs and Madsen* [1992] to derive a nonlinear diffusion equation for the free surface elevation. *Friedrichs and Madsen* [1992] obtained approximate analytical solutions for this equation by expanding the time-varying geometric parameters. In particular, first, a solution is acquired considering a constant diffusion coefficient. Then, this solution is applied to evaluate the time variation of the diffusion coefficient, retaining thus a linear diffusion equation governing the free surface elevation.

Recently, *Van Oyen et al.* [2012] introduced a simplified model for frictionally dominated tidal flows. The model expands the relevant variables in terms of the small parameters appearing in the dimensionless depth-averaged conservation equations of mass and momentum. Combining momentum and mass conservation at each order of approximation, this expansion leads to a linear diffusion equation for the variation of the free surface elevation with respect to the spatially averaged surface level. Flow velocities are prescribed by momentum balance at the considered order of approximation, relating the flow to the gradient in the free surface elevation and known terms. *Van Oyen et al.* [2012] showed that the procedure reasonably describes the flow field during the entire period of the tidal cycle that the intertidal platform is wetted; contrary to the approach suggested by *Rinaldo et al.* [1999] which implies that the flow velocity approaches infinity when the depth goes to zero. Moreover, *Van Oyen et al.* [2012] discussed the ability of the approach to account for spatially uniform variations of the friction coefficient.

1.3. Research Objectives

As illustrated by Figure 1, friction on tidal platforms is often characterized by a nonuniform spatial distribution associated with the spatial variations in vegetation and macro algae cover on salt marshes and tidal flats. These patterns strongly influence the flow field and, consequently, erosion and sedimentation processes. Within vegetation patches, the flow velocities are reduced owing to the increased friction, while the water is partly forced to flow around the patch. At the patch boundary this leads to increased flow velocities, and hence to higher erosion capacity [e.g., *Zong and Nepf*, 2010; *Vandenbruwaene et al.*, 2011], possibly determining channel initiation around and in between vegetation patches [*Temmerman et al.*, 2007].

Since *Van Oyen et al.* [2012] considered only a spatially homogeneous friction, the central research objective of the present manuscript is to examine the potential of the model to describe the effects of vegetation patches, leading to a nonuniform spatial distribution of the friction. In particular, the manuscript aims to quantify and discuss in detail the limitations of the approach and analyze the occurrence of these

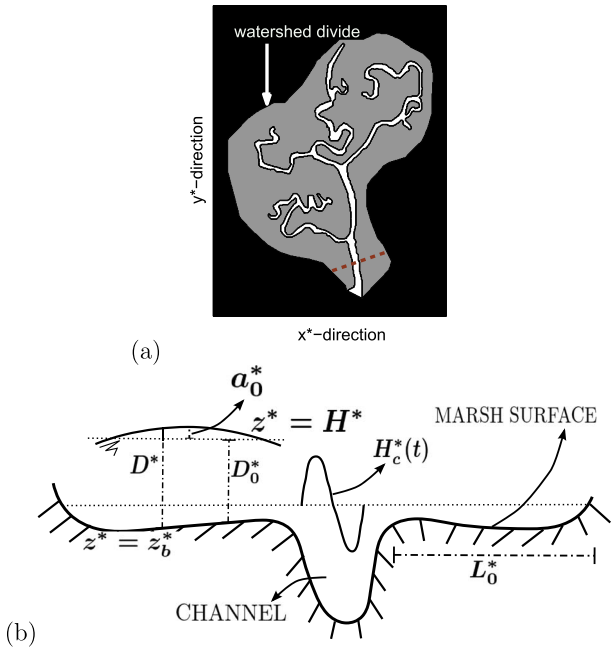

Figure 2. (a) Sketch of a typical salt marsh domain, based on a tidal network observed in the Venice Lagoon [*D'Alpaos*, 2011]. The channel network is in white, while the gray area represents the intertidal platform. The platform is bounded by the region in black, which can be a physical boundary or the watershed divide. (b) Sketch of the geometry across the dashed line depicted in Figure 2a. The variables illustrated in Figure 2b are denoted in the text.

limitations in relation with the introduced assumptions. In addition, a novel solution procedure (based on a Fourier expansion in time) is introduced and the influence of the nonlinearity of friction is examined. Finally, keeping in mind the intention to provide a reliable tool to investigate the long-term evolution of tidal wetlands, the implications of the model limitations for the ability to describe quantitatively morphological changes are analyzed. In particular, a detailed comparison is made between the changes in the bed elevation after one tidal cycle on the intertidal platform, based on flow velocities obtained with a numerical model and those resulting from the simplified procedure.

The paper is organized as follows. In the next section, the model formulation (section 2) is described, after which the solution procedure is specified (section 3). The discussed formulation (section 2) follows closely that described by *Van Oyen et al.* [2012] but is elaborated here in more detail to clarify the derivation. Next, the ability of the approach to model relevant features of the hydrodynamics on the intertidal platform is analyzed. In section 5, the overall results are discussed, describing the advantages and disadvantages of the proposed approach, while section 6 provides the conclusions of the work.

2. Model Formulation

We aim at providing a reliable, simplified description of the flow field on an intertidal platform adjacent to a relatively short tidal channel. The system is forced by a semidiurnal tidal wave with frequency ω^*, amplitude A_p^* and a prescribed averaged elevation (mean sea level, MSL). Owing to the short length of the tidal channel and the larger friction on the intertidal platform, the tide is assumed to propagate quasi-statically (i.e., nearly instantaneously) in the channel. Hence, in this region, the free surface elevation $H_c^*(t^*)$ is considered spatially uniform and equal to the time-varying water level (t^* denotes time) imposed at the channel inlet. The flow field on the intertidal platform is thus driven by the difference in the free surface elevation occurring at the edge between the intertidal platform and the channel, i.e., at this location the free surface is imposed to equal $H_c^*(t)$ as boundary condition. A no-flux condition is imposed at the end of the intertidal platform (both in the x^* and y^* direction), which represents either the presence of a physical boundary or a watershed divide (see Figure 2 for a sketch of the model domain).

We consider an orthogonal coordinate system with the x^* and y^* axes in the horizontal directions, while the z^* axis, pointing upward, denotes the vertical direction (Figure 2). Hereinafter, a star will be used to denote dimensional quantities. The equations governing the flow field on the intertidal platform are the depth-averaged momentum and mass conservation equations [e.g., *Dronkers*, 1964]:

$$\frac{\partial u^*}{\partial t^*} + \left(u^* \frac{\partial u^*}{\partial x^*} + v^* \frac{\partial u^*}{\partial y^*} \right) = -g^* \frac{\partial H^*}{\partial x^*} - g^* \frac{u^* |\boldsymbol{u}^*|}{\chi^{*2} D^*}, \tag{1}$$

$$\frac{\partial v^*}{\partial t^*} + \left(u^* \frac{\partial v^*}{\partial x^*} + v^* \frac{\partial v^*}{\partial y^*} \right) = -g^* \frac{\partial H^*}{\partial y^*} - g^* \frac{v^* |\boldsymbol{u}^*|}{\chi^{*2} D^*}, \tag{2}$$

$$\frac{\partial H^*}{\partial t^*} + \frac{\partial}{\partial x^*} (D^* u^*) + \frac{\partial}{\partial y^*} (D^* v^*) = 0. \tag{3}$$

Here u^* and v^* are the depth-averaged flow velocities in the x^* and y^* direction, respectively. Furthermore, H^* denotes the free surface elevation, g^* the gravitational acceleration, and D^* the local depth (i.e., $D^* = H^* - z_b^*$), with z_b^* the elevation of the intertidal platform. The last term on the right-hand side of equations (1) and (2) represents the influence of friction on the momentum balance, described by introducing a Chézy friction law, with χ^* the Chézy coefficient. In the following, the impact of vegetation variations on the flow field is mimicked by varying the value of the friction coefficient. The model can, however, be adapted to describe more directly the impact of vegetation on the flow field, by relating the Chézy coefficient to the physical properties of vegetation species encroaching (or populating) the marsh platform (e.g., stem density and height).

In order to rewrite the dimensional conservation equations in dimensionless form, we consider length-, velocity- and time-scales, typical of the problem. In particular, we introduce the following nondimensional variables:

$$(x, y) = \frac{(x^*, y^*)}{L_0^*}, \quad t = t^* \omega^*, \quad (D, H) = \frac{(D^*, H^*)}{D_0^*}, \tag{4}$$

$$\chi = \frac{\chi^*}{\chi_0^*} \quad \text{and} \quad (u, v) = \frac{(u^*, v^*)}{U_0^*}, \tag{5}$$

with ω^* the angular frequency of the dominant component of the tidal wave, L_0^* the typical length of the intertidal platform, D_0^* a characteristic water depth, U_0^* a representative flow velocity, and χ_0^* a typical value of the friction Chézy coefficient.

The free surface elevation is split into two contributions: a spatially constant one $\xi^*(t^*)$ given by the spatially averaged elevation and a variable one $\zeta^*(x^*, y^*, t^*)$, which expresses the variation of the local free surface with respect to the mean. Observing that the scale a_0^* (see Figure 2) of the free surface variations (occurring free surface level with respect to its spatially averaged value) is usually much smaller than the characteristic water depth, we write

$$H = \xi(t) + \epsilon \zeta(x, y, t), \tag{6}$$

with $\epsilon = a_0^*/D_0^*$ a small dimensionless parameter. The dimensionless form of the governing equations, taking into account equations (4)–(6), reads as follows:

$$\alpha \left\{ \frac{\partial u}{\partial t} + r \left(u \frac{\partial u}{\partial x} + v \frac{\partial u}{\partial y} \right) \right\} = -\epsilon \frac{\partial \zeta}{\partial x} - \gamma \frac{u |\boldsymbol{u}|}{\chi^2 D}, \tag{7}$$

$$\alpha \left\{ \frac{\partial v}{\partial t} + r \left(u \frac{\partial v}{\partial x} + v \frac{\partial v}{\partial y} \right) \right\} = -\epsilon \frac{\partial \zeta}{\partial y} - \gamma \frac{v |\boldsymbol{u}|}{\chi^2 D}, \tag{8}$$

$$\frac{\mathrm{d}\xi}{\mathrm{d}t} + \epsilon \frac{\partial \zeta}{\partial t} + r \left\{ \frac{\partial}{\partial x} (Du) + \frac{\partial}{\partial y} (Dv) \right\} = 0, \tag{9}$$

where the dimensionless parameters α, γ, and r are given by

$$\alpha = \frac{U_0^* \omega^* L_0^*}{g^* D_0^*}, \quad r = \frac{U_0^*}{\omega^* L_0^*}, \quad \gamma = \frac{U_0^{*2} L_0^*}{(\chi_0^* D_0^*)^2}. \tag{10}$$

In order to simplify the analysis, as a first approximation, we linearize the friction terms [e.g., *Schuttelaars and de Swart*, 1999]. Following the energy criterion first introduced by *Lorentz* [1926], we consider the following:

$$\frac{u |\boldsymbol{u}|}{\chi^2 D} = \frac{\lambda u}{\chi^2 D}, \qquad \frac{v |\boldsymbol{u}|}{\chi^2 D} = \frac{\lambda v}{\chi^2 D}, \tag{11}$$

with

$$\lambda = \frac{8}{3\pi}. \tag{12}$$

In section 5 the implications of this approximation are discussed.

The order of magnitude of the dimensionless parameters appearing in (7)–(9) are estimated on the basis of field observations [see *Rinaldo et al.*, 1999, Table A1 and references therein]. In particular, we observe that typical velocities and length scales of the flow field occurring on intertidal platforms are in the ranges

0.1–0.2 m s^{-1} and 250–1000 m, respectively. Moreover, χ_0^* is approximately 10 $m^{1/2}$ s^{-1}, D_0^* about 1 m, and a_0^* a few centimeters. Finally, considering a semidiurnal tidal wave, $\omega^* \approx 10^{-4}$ s^{-1}. As a consequence

$$\alpha \sim \mathcal{O}(10^{-3}),\ r \sim \mathcal{O}(1),\ \gamma \sim \mathcal{O}(10^{-1}),\ \epsilon \sim \mathcal{O}(10^{-2}), \tag{13}$$

indicating that $\alpha \ll \gamma$, $\epsilon < \gamma$ and $\alpha < \epsilon$.

Motivated by this result, we seek for solutions to equations (7)–(9), by expanding the relevant variables in the small parameters ϵ and α:

$$\begin{aligned}(u, v, \zeta, \xi, D) = (u_0, v_0, \zeta_0, \xi_0, D_0) + \epsilon\,(u_{11}, v_{11}, \zeta_{11}, \xi_{11}, D_{11}) \\ + \alpha\,(u_{12}, v_{12}, \zeta_{12}, \xi_{12}, D_{12}) + \epsilon^2(u_{21}, v_{21}, \zeta_{21}, \xi_{21}, D_{21}) \\ + \epsilon\alpha(u_{22}, v_{22}, \zeta_{22}, \xi_{22}, D_{22}) + \alpha^2(u_{23}, v_{23}, \zeta_{23}, \xi_{23}, D_{23}) \\ + \epsilon^3(u_{31}, v_{31}, \zeta_{31}, \xi_{31}, D_{31}) + h.o.t.,\end{aligned} \tag{14}$$

where *h.o.t.* denotes higher order terms. In (14), the variables u, v, ζ, and D can vary with time and space, while ξ is a function of time only. Here we note that the observation that $\alpha \ll \gamma$ could also motivate to consider an expansion in ϵ only and neglect the inertial terms, which is a common assumption [e.g., *Toffolon and Lanzoni*, 2010]. Yet we retain these terms in the following as it facilitates the analysis of their influence on the flow field which we present in section 5.2.

Applying expansion (14) to the momentum and mass balance equations (7)–(9), at the leading order of approximation $\mathcal{O}(\epsilon^0)$, we retain

$$\frac{\gamma\lambda}{\chi^2 D_0}(u_0, v_0) = 0, \tag{15}$$

$$\frac{\mathrm{d}\xi_0}{\mathrm{d}t} = 0. \tag{16}$$

implying a quasi-static propagation of the tidal wave, i.e., that the spatially averaged elevation ξ_0 is constant in time and $u_0 = v_0 = 0$.

At the order $\mathcal{O}(\epsilon)$, the momentum balance yields

$$\frac{\partial\zeta_0}{\partial x} = -\frac{\gamma\lambda}{\chi^2}\left(\frac{u_{11}}{D_0} - \frac{u_0 D_{11}}{D_0^2}\right), \quad \frac{\partial\zeta_0}{\partial y} = -\frac{\gamma\lambda}{\chi^2}\left(\frac{v_{11}}{D_0} - \frac{v_0 D_{11}}{D_0^2}\right), \tag{17}$$

and, therefore,

$$u_{11} = -\frac{\chi^2 D_0}{\gamma\lambda}\left(\frac{\partial\zeta_0}{\partial x}\right), \quad v_{11} = -\frac{\chi^2 D_0}{\gamma\lambda}\left(\frac{\partial\zeta_0}{\partial y}\right). \tag{18}$$

Furthermore, at order ϵ, conservation of mass provides

$$\frac{\mathrm{d}\xi_{11}}{\mathrm{d}t} + \frac{\partial\zeta_0}{\partial t} + r\left[\frac{\partial}{\partial x}\left(u_{11}D_0\right) + \frac{\partial}{\partial y}\left(v_{11}D_0\right)\right] = 0, \tag{19}$$

which, recalling (18), leads to

$$\frac{\mathrm{d}\xi_{11}}{\mathrm{d}t} + \frac{\partial\zeta_0}{\partial t} - r\left[\frac{\partial}{\partial x}\left(\frac{\chi^2 D_0^2}{\gamma\lambda}\frac{\partial\zeta_0}{\partial x}\right) + \frac{\partial}{\partial y}\left(\frac{\chi^2 D_0^2}{\gamma\lambda}\frac{\partial\zeta_0}{\partial y}\right)\right] = 0. \tag{20}$$

Here $\mathrm{d}\xi_{11}/\mathrm{d}t$ denotes the forcing term and is evaluated by relating the spatially averaged water surface elevation on the intertidal platform $\xi(t)$ to the channel water level $H_c(t)$ as

$$H_c(t) = \xi_0 + \epsilon\xi_{11}(t). \tag{21}$$

Equation (21) implies that we do not account for the spatial variation of the wetting/drying process occurring on the platform. Furthermore, it describes that we choose to represent the time-varying and time-averaged parts of the tidal wave in the channel by ξ_0 and ξ_{11}, respectively. This particular choice is

Table 1. Expressions of the Terms Appearing in (22) and (23) at the Various Orders of Approximation

	Υ	$K^x_{k,l}$	$K^y_{k,l}$	$F_{k,l}$
α	0	0	0	-
ϵ^2	$-\frac{\chi^2 D_0}{\gamma\lambda}$	$\frac{u_{11}D_{11}}{D_0}$	$\frac{v_{11}D_{11}}{D_0}$	$2r\left[\frac{\partial}{\partial x}\left(u_{11}D_{11}\right)+\frac{\partial}{\partial y}\left(v_{11}D_{11}\right)\right]$
$\alpha\epsilon$	$-\frac{\chi^2 D_0}{\gamma\lambda}$	$-\frac{\chi^2 D_0}{\gamma\lambda}\frac{\partial u_{11}}{\partial t}$	$-\frac{\chi^2 D_0}{\gamma\lambda}\frac{\partial v_{11}}{\partial t}$	$-r\left[\frac{\partial}{\partial x}\left(\frac{\chi^2 D_0^2}{\gamma\lambda}\frac{\partial u_{11}}{\partial t}\right)+\frac{\partial}{\partial y}\left(\frac{\chi^2 D_0^2}{\gamma\lambda}\frac{\partial v_{11}}{\partial t}\right)\right]$
α^2	0	0	0	-
ϵ^3	$-\frac{\chi^2 D_0}{\gamma\lambda}$	$\frac{u_{21}D_{11}}{D_0}+\frac{u_{11}D_{21}}{D_0}$	$\frac{v_{21}D_{11}}{D_0}+\frac{v_{11}D_{21}}{D_0}$	$r\left[\frac{\partial}{\partial x}\left(2u_{21}D_{11}+2u_{11}D_{21}-\frac{u_{11}D_{11}^2}{D_0}\right)\right]$
		$-\frac{u_{11}D_{11}^2}{D_0^2}$	$-\frac{v_{11}D_{11}^2}{D_0^2}$	$+r\left[\frac{\partial}{\partial y}\left(2v_{21}D_{11}+2v_{11}D_{21}-\frac{v_{11}D_{11}^2}{D_0}\right)\right]$

consistent with the constraint that ξ_0 is constant (and other constraints obtained at higher orders, see below). In addition, it is worthy to note that a particular choice on the relation between H_c and the different orders of approximation in ξ does not influence the overall dynamics since the resulting flow field is a linear combination of all the orders of approximation.

Equation (20) thus describes a linear diffusion equation for the variations $\zeta_0(x, y, t)$ of the local free surface elevation with respect to the mean. The solution procedure providing the time variation of $\zeta_0(x, y, t)$ is described in the next section. Once obtained, the flow velocities are readily evaluated with equation (18).

The flow field at higher orders of approximation is governed by similar relationships. In general, the momentum balance allows to determine the flow velocity as a combination of the gradient of the free surface elevation and known terms ($K^x_{k,l}$ and $K^y_{k,l}$):

$$u_{k,l} = \Upsilon\frac{\partial\zeta_{k-1,l}}{\partial x} + K^x_{k,l}, \quad v_{k,l} = \Upsilon\frac{\partial\zeta_{k-1,l}}{\partial y} + K^y_{k,l}. \tag{22}$$

Here the subscripts (k, l) denote the order of approximation with respect to the parameters ϵ and α, respectively. Substituting these expressions in the problem obtained at the considered order of approximation from the mass conservation equation leads to a linear diffusion equation of the form

$$F_{k,l} + \frac{\partial\zeta_{i-1,j}}{\partial t} - r\left[\frac{\partial}{\partial x}\left(\frac{\chi^2 D_0^2}{\gamma\lambda}\frac{\partial\zeta_{i-1,j}}{\partial x}\right)+\frac{\partial}{\partial y}\left(\frac{\chi^2 D_0^2}{\gamma\lambda}\frac{\partial\zeta_{i-1,j}}{\partial y}\right)\right] = 0. \tag{23}$$

Equation (23) can be solved following the same procedure as for (20), specified in detail in section 3, after which the flow velocity at each order of approximation is determined using (22). The expressions for the terms $\Upsilon, K^x_{k,l}, K^y_{k,l}$, and $F_{k,l}$ appearing in (22) and (23) are summarized in Table 1 for each order of approximation.

Note that the relations obtained at the orders α and α^2 provide an exception to (22) and (23). In particular, at these orders, it is found that $u_{12} = v_{12} = 0$ and $u_{23} = v_{23} = 0$, while the approximate expression of the mass conservation describes that ξ_{12} and ξ_{23} are both constant.

3. Solution Procedure

The linear character of the sequence of diffusion equations for the free surface elevation (equations (20) and (23)), resulting from the introduced expansion, allows us to exploit the periodic nature of the flow field over the intertidal platform (as induced by a tidal wave in the adjacent channel) within the solution procedure. In particular, the time dependence of the relevant parameters can be described as a Fourier series in time, such that

$$\left(\frac{\mathrm{d}\xi_{11}}{\mathrm{d}t}, \zeta_{k,l}, u_{k,l}, v_{k,l}\right) = \sum_{n=0}^{N}\left(\phi^{(n)}, \zeta^{(n)}_{k,l}, u^{(n)}_{k,l}, v^{(n)}_{k,l}\right)e^{in\mathrm{t}} + c.c. \quad , \tag{24}$$

where *c.c.* denotes the complex conjugate.

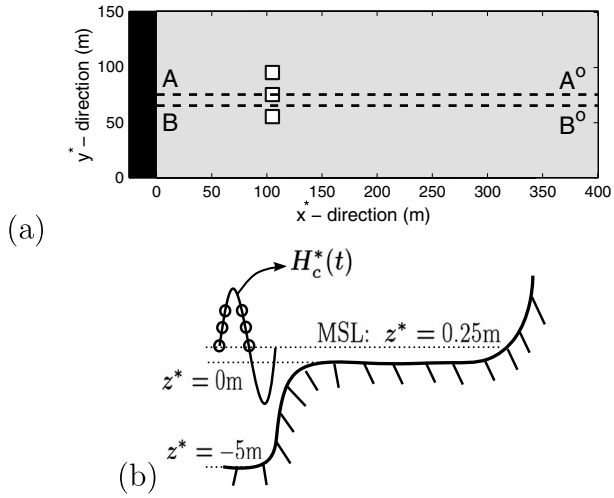

Figure 3. (a) Spatial distribution of the friction coefficient on the considered idealized intertidal domain, exhibiting three 10 × 10 m vegetated patches (white area) characterized by a Strickler roughness coefficient $K_s^* = 10$ m$^{1/3}$ s^{-1}. On the platform next to the patches (grey area), K_s^* is set equal to 25 m$^{1/3}$ s^{-1}, while K_s^* equals 50 m$^{1/3}$ s^{-1} in the channel flanking the intertidal platform. In Figure 3a, the location of the adjacent channel is depicted by the black area on the left. The corresponding values of the Chézy friction coefficient are given by $\chi^* = K_s^*(H_c^*(t) - z_b^*)^{1/6}$. The dashed lines represent the transects A-A^0 and B-B^0 considered in the plots of Figures 5, 6, 9, 12, 13, 15, 16, and 17. (b) Sketch of a transect perpendicular to the channel axis. The instants of the tidal cycle specifically considered in the subsequent figures are denoted by circles.

Substituting (24) into the equations governing the problem at the first order of approximation (equations (18)–(20)), we obtain for each qth harmonic

$$u_{11}^{(q)} = -\frac{\chi^2 D_0}{\gamma\lambda}\frac{\partial\zeta_0^{(q)}}{\partial x}, \qquad v_{11}^{(q)} = -\frac{\chi^2 D_0}{\gamma\lambda}\frac{\partial\zeta_0^{(q)}}{\partial y}, \tag{25}$$

$$\phi^{(q)} + \imath q\zeta_0^{(q)} = \frac{r}{\gamma\lambda}\left[\frac{\partial}{\partial x}\left(\chi^2 D_0^2\frac{\partial\zeta_0^{(q)}}{\partial x}\right) + \frac{\partial}{\partial y}\left(\chi^2 D_0^2\frac{\partial\zeta_0^{(q)}}{\partial y}\right)\right]. \tag{26}$$

Equation (26) thus prescribes the amplitude of the spatial variation of the free surface elevation for each harmonic q at $\mathcal{O}(\epsilon)$. In order to obtain a solution of $\zeta_0^{(q)}$ on a generic domain with possible depth and friction variations, equation (26) is spatially discretized with a finite difference scheme. The resulting system of equations is solved using the open source computational package ILUPACK [*Bollhoefer and Saad*, 2006]. The amplitude of the qth harmonic of the flow velocity is then readily evaluated with equation (25).

Similarly, considering (24) at the higher orders of approximation (i.e., equations (22) and (23)) leads to

$$u_{k,l}^{(q)} = \Upsilon\frac{\partial\zeta_{k-1,l}^{(q)}}{\partial x} + K_{k,l}^{x,(q)}, \quad v_{k,l}^{(q)} = \Upsilon\frac{\partial\zeta_{k-1,l}^{(q)}}{\partial y} + K_{k,l}^{y,(q)}, \tag{27}$$

$$F_{k,l}^{(q)} + \imath q\zeta_{k-1,l}^{(q)} = \frac{r}{\gamma\lambda}\left[\frac{\partial}{\partial x}\left(\chi^2 D_0^2\frac{\partial\zeta_{k-1,l}^{(q)}}{\partial x}\right) + \frac{\partial}{\partial y}\left(\chi^2 D_0^2\frac{\partial\zeta_{k-1,l}^{(q)}}{\partial y}\right)\right], \tag{28}$$

for each qth harmonic. Similar to the solution procedure specified for $\mathcal{O}(\epsilon)$, the values of $\zeta_{k-1,l}$ are obtained by spatially discretizing equation (28) with a finite difference scheme and solving the resulting system of equations with ILUPACK. Then, the amplitudes of the harmonics of the flow velocity can be computed with equation (27).

Here it is worth pointing out that, despite considering only a semidiurnal tidal wave in the channel, characterized by one frequency ($n = 1$), higher harmonics need to be taken into account to describe the flow field on the platform. In particular, during the periods of the tidal cycle when the water level is below the intertidal platform, the forcing of the flow field on the platform vanishes such that the rate of change of the free surface elevation in the channel (which drives the flow field on the platform) is discontinuous in time. Hence, in order to adequately describe $\mathrm{d}\xi_{11}(t)/\mathrm{d}t$ by means of a Fourier series, a number of higher frequencies need to be considered. In the results presented in the following section, the number N of terms considered in the Fourier series is taken equal to 35. Note, however, that in equations (27) and (28), frequencies higher than N, which occur due to interactions between various variables, are neglected.

4. Results

4.1. Comparison With a Numerical Model

A first evaluation of the ability of the present approximate approach to describe the effects of spatial variations in the friction coefficient χ is performed by a comparison with the flow field predicted by the

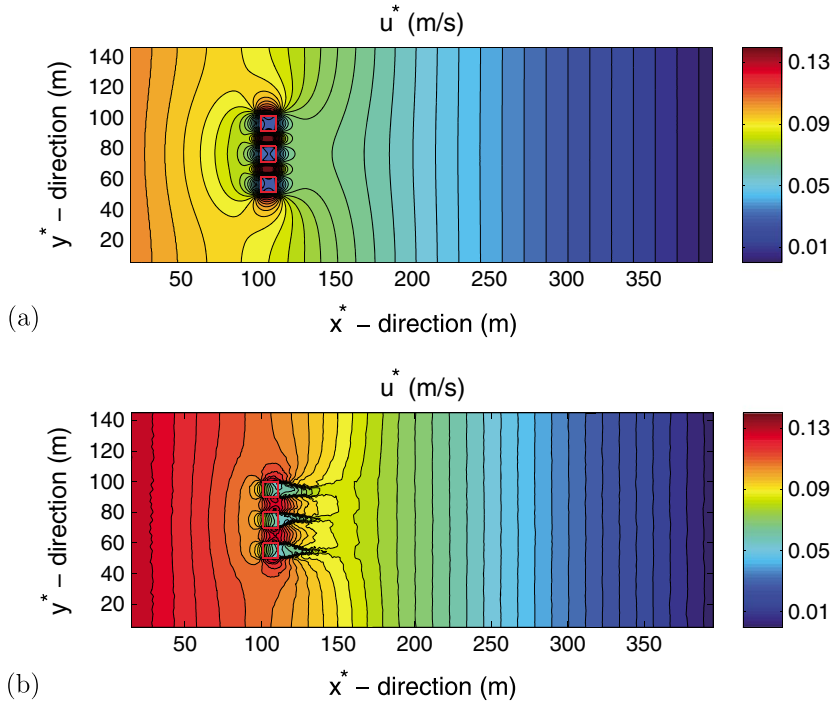

Figure 4. Spatial distribution of the x^* axis velocity component u^* (i.e., normal to the channel axis), during the flooding phase of the tide, when the tidal level is 0.5 m above the intertidal platform elevation. The red lines indicate the border of the vegetated patches. (a) Simplified model results; (b) numerical model results.

full-fledged numerical model (hereinafter denoted by WWTM) introduced by *Defina* [2000] and further developed and validated by *Carniello et al.* [2005, 2011].

To facilitate the comparison, an idealized domain is considered. In particular, a rectangular tidal platform with uniform elevation is considered, which, on the left side, is aligned with a tidal channel where the tidal wave elevation $H_c^*(t^*)$ is imposed (see Figure 3). The elevation of the tidal platform z_b^* is considered the reference vertical level (i.e., $z_b^* = 0$), and the bed of the channel is 5 m below the tidal platform ($z^* = -5$ m). The tidal channel is 20 m wide (in the x^* direction) and 150 m long (in the y^* direction), while the tidal platform is assumed 400 m wide. Moreover, the origin of the x^* and y^* axes is set at the intersection between the tidal platform and the channel, at the lower end of the computational domain, see Figure 3a. In this figure, the black area on the left of the domain represents the tidal channel adjacent to the tidal platform and the dashed lines illustrate the transects A-A^0 and B-B^0 which are considered in the figures presented in sections 4 and 5.

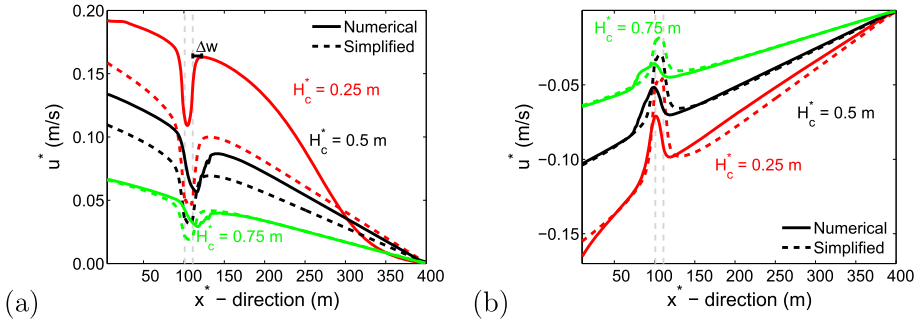

Figure 5. The x^*axis velocity component u^* (i.e., normal to the channel axis) plotted as a function of x^* along the transect A-A^0 reported in Figure 3 at various instants of the (a) flood and (b) ebb phase. The vertical gray lines denote the position of the vegetated patches. The continuous lines refer to the numerical results and the dashed lines to the simplified solution.

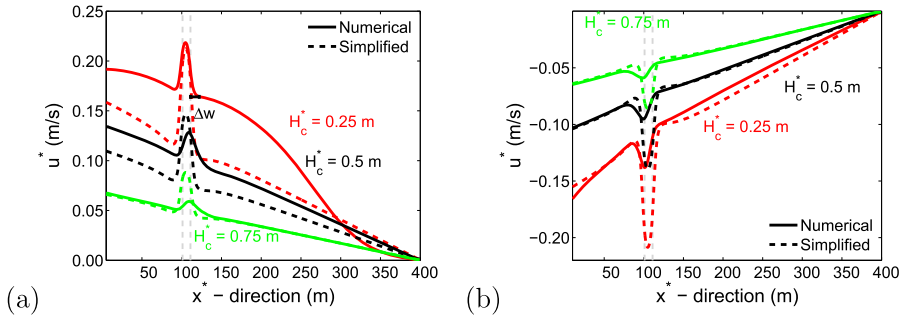

Figure 6. The x^*axis velocity component u^* (i.e., normal to the channel axis) plotted as a function of x^* along the transect B-B^0 reported in Figure 3 at various instants of the (a) flood and (b) ebb phase. The vertical gray lines denote the position of the vegetated patches. The continuous lines refer to the numerical results and the dashed lines to the simplified solution.

Vegetation patches are mimicked by adjusting the friction coefficient in some portions of the domain on the platform such that friction is increased in these areas. In order to relate the Strickler coefficient (K_s^* (m$^{1/3}$ s^{-1})) used in the WWTM model to the Chézy coefficient (χ^* (m$^{1/2}$ s^{-1})) considered in the present approach, we recall that the Chézy friction coefficient can be expressed in terms of the Strickler coefficient, depending only on the overall bed roughness and depth, through the relation $\chi^* = K_s^*(H_{re}^* - z_b^*)^{1/6}$, with H_{re}^* equal to 0.25 m.

In the domain considered in the following applications, the Strickler coefficient is set equal to 10 m$^{1/3}$ s^{-1} (more friction) in the white (vegetated) patches and is considered equal to 25 m$^{1/3}$ s^{-1} (less friction) on the platform next to the patches, see Figure 3. In the channel flanking the tidal platform, K_s^* is equal to 50 m$^{1/3}$ s^{-1} (black region in Figure 3a). Furthermore, the patches are assumed as a square portion of the domain with a side length Δ_p of 10 m, while the distance between the patches Δ_b is set equal to 10 m.

Figure 4 shows the spatial distribution of the velocity component u^* normal to the channel axis (i.e., in the x^* direction), obtained by using the approximate approach (Figure 4a) and the complete finite element model (Figure 4b). The results refer to the flooding phase of the tide, when the mean tidal level is 0.5 m above the bottom elevation of the intertidal platform. The flow field is driven by a semidiurnal tidal wave, imposed in the channel, characterized by an amplitude A_p^* of 1 m and an averaged value (MSL) of 0.25 m. Both models predict that the velocity strongly reduces within the vegetated patches, while it is significantly enhanced in between the patches and along their edges, thus indicating good qualitative agreement.

A more quantitative comparison between the results provided by the present simplified model and the complete numerical model is illustrated in Figures 5 and 6, which show the value of u^* at several instants of the tidal cycle, along the dashed lines (depicted in Figure 3) passing through the middle patch and in between two patches, respectively. The timing of the considered instants is illustrated in Figures 3b (circles on the sine curve representing the imposed tide).

Overall, a good quantitative agreement is found during the ebb tide and at the later stages of the flooding tide (i.e., when $H_c^* \geq 0.5$ m). At the beginning of the flooding stage, however, larger differences occur, in particular near the channel edge ($x^* = 0$ m), where the approximate approach underestimates u^*, and in the proximity of the intertidal platform divide ($x^* = 400$ m), where the simplified model predicts slightly larger values of u^*. This behavior is also reflected in the value of r_{ms}, the normalized root mean square, which

Table 2. Values of r_{ms} at Several Stages of the Tidal Cycle, Computed by Using the Values of u^* Along the Section A-A^0 (Left Part) and Along the Section B-B^0 (Right Part of the Table)

	Section A-A^0		Section B-B^0	
H_c^* (m)	Flooding Phase	Ebb Phase	Flooding Phase	Ebb Phase
0.25	0.2194	0.0654	0.1784	0.0825
0.5	0.1333	0.0567	0.1316	0.0836
0.75	0.0599	0.0502	0.0788	0.0844

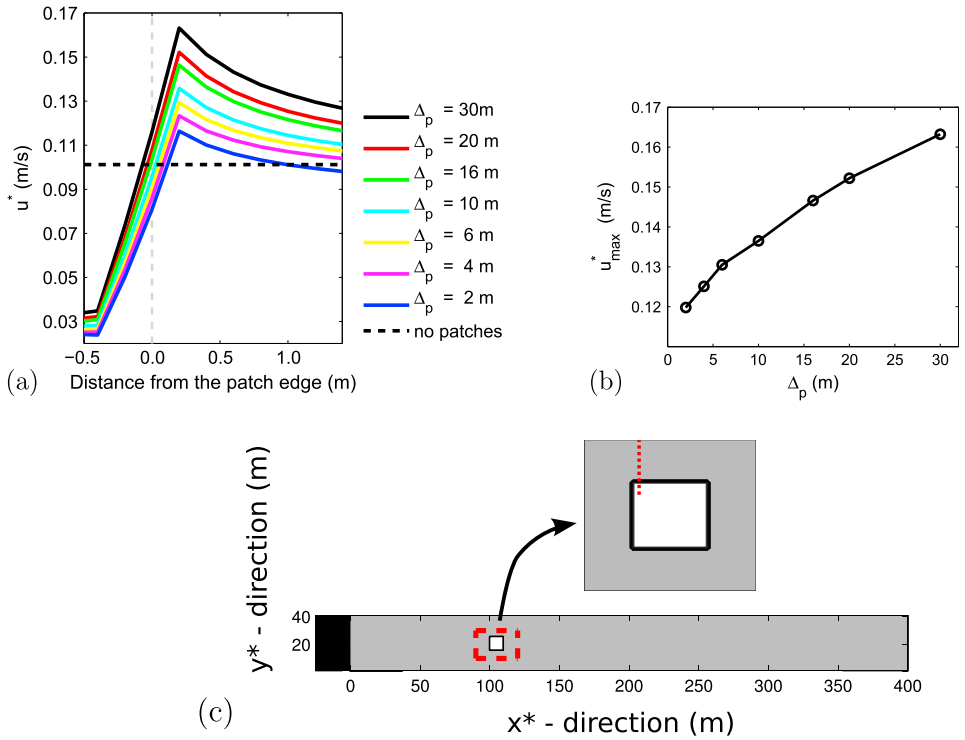

Figure 7. (a) The component of the flow velocity normal to the channel axis u^* plotted as a function of the distance from the patch edge along a transect parallel to the channel (i.e., in the y^* direction), located half a meter behind the edge of the vegetated patch, for different values of the patch size Δ_p. (b) Maximum value of u^* next to the patch versus Δ_p. (c) Illustration of the location of the transect (dashed red line in the top plot) considered in Figure 7a. Both Figures 7a) and 7b refer to the flooding phase, when $H_c^* = 0.5$ m.

quantitatively evaluates the difference between the numerical and approximate approach. In particular, the value of r_{ms} decreases toward tidal reversal during the flooding phase and keeps low during the entire ebb phase, see Table 2. In addition, Figures 5a and 6a, respectively, show that downstream of the vegetated patches u^* increases/decreases more rapidly when adopting the approximate approach. As immediately emerges by considering the distance Δw between the edge of a vegetation patch and the downstream local maxima of u^*, the wake behind a vegetated patch is smaller when using the simplified model. Finally, the results also indicate that the impact of the friction variations on the flow field is overestimated by the simplified model. In particular, within the patch, the reduction of the flow field is larger for the approximate approach than for the numerical model, while with the simplified model, the flow velocity is more strongly amplified next to the patch.

Comparable results (not shown) are obtained at different instants of the tidal cycle and considering larger and smaller patch dimensions; i.e., Δ_p equal to 5 m, 30 m, and 50 m. The distance between the patches in all these cases is set equal to the width of the square patch.

4.2. Qualitative Comparison With Laboratory Experiments

The performance of the approximate solution is also investigated by a qualitative comparison with laboratory experiments performed by *Vandenbruwaene et al.* [2011]. The comparison is necessarily qualitative since the laboratory experiments consider a steady flow while the model is conceived to account for a tidal flow. Hence, a quantitative comparison would require a reformulation of the problem, which falls beyond the scope of the present analysis.

The experiments carried out by *Vandenbruwaene et al.* [2011] reveal that the impact of vegetation patches on the flow field is scale dependant. In particular, *Vandenbruwaene et al.* [2011] found that the maximum flow velocity, next to the patches, increases with the dimension of the patch. Moreover, it is found that the presence of two patches next to each other induces a certain flow interaction such that the difference Δ_{vel}

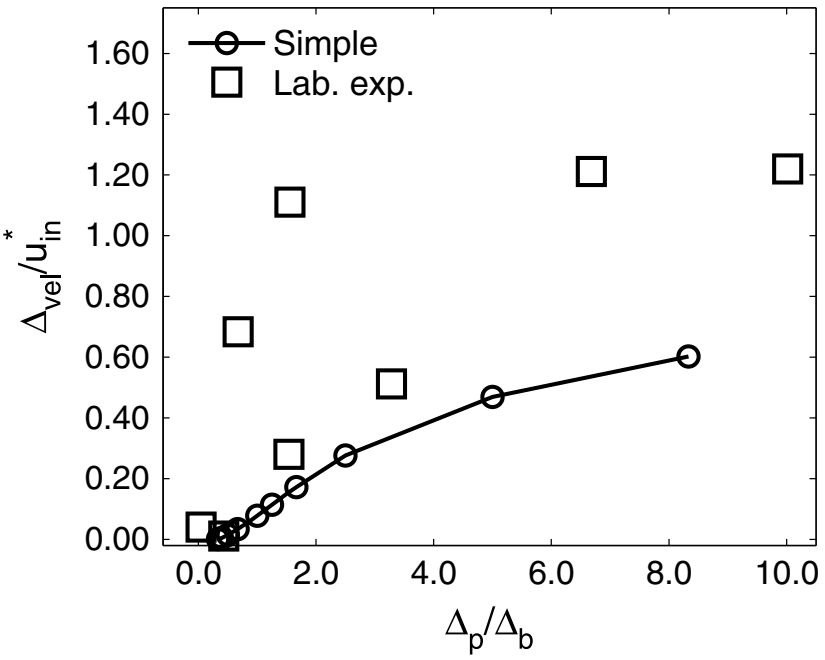

Figure 8. The difference Δ_{vel} between the velocities (in the x^* direction) observed in between two adjacent patches and next to a patch (30 cm from the patch border), normalized with the velocity u^*_{in}, plotted as a function of the ratio of the patch size length, Δ_p, with the interpatch distance Δ_b. The velocity u^*_{in} (= 0.1 m s^{-1}) denotes the local velocity which occurs if no friction variations are considered. The squares illustrate the results derived from laboratory experiments as reported by *Vandenbruwaene et al.* [2011].

between the increase in velocity in between the patches and the increase observed next to the patches, becomes larger when the interpatch distance Δ_b decreases.

Figures 7 and 8 show that all these experimentally observed features are qualitatively well reproduced by the model. In Figure 7a, the value attained by u^* is illustrated as a function of the distance from the patch edge along a section parallel to the channel (i.e., in the y^* direction), half a meter behind the leading edge of the patch, considering different values of patch dimension Δ_p. The plotted velocity is obtained during the flooding phase when H^*_c equals 0.5 m, by considering the same domain of Figure 3. The considered patch is located on the tidal platform (see Figure 7c), 100 m from the channel edge, in the x^* direction; while the distance from the patch edge to the boundary, in the y^* direction, is set equal to $\frac{3}{2}\Delta_p$ for each experiment, in order to minimize scale-dependent boundary effects. In addition, Figure 7b illustrates the maximum amplitude of u^* observed in the domain close to the patch. Figures 7a and 7b show that the simplified approach correctly reproduces the increase in the maximum flow velocity next to the patch with increasing patch dimensions in accordance with the laboratory experiments.

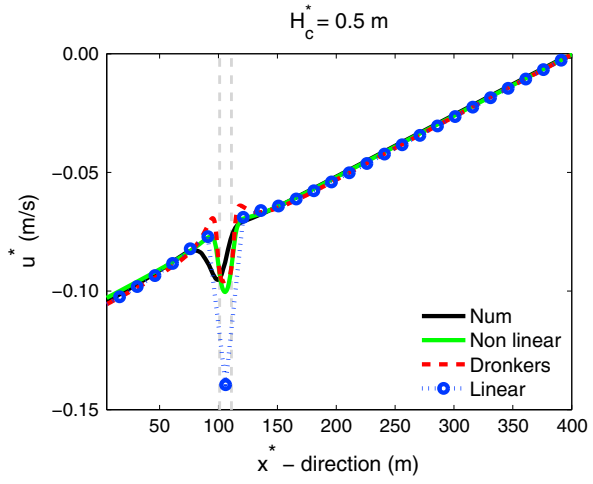

Figure 9. Comparison of the velocity u^* in the direction normal to the channel along the transect B-B^0 of Figure 3, with nonlinear friction (green line), linearized friction (blue circles with dashed line), friction modeled as proposed by *Dronkers* [1964] (red dashed line), and numerical model (black line) during the ebb phase (H^*_c = 0.5 m). The gray lines indicate the position of the vegetated patch.

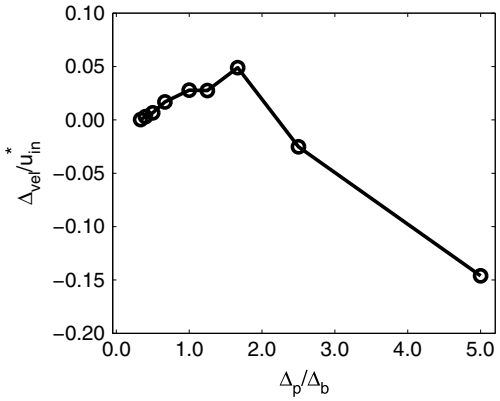

Figure 10. The difference Δ_{vel} between the velocities (in the x^* direction) observed in between two adjacent patches and next to a patch (30 cm from the patch border), normalized with the velocity u_{in}^*, plotted as a function of the ratio of the patch size length, Δ_p, with the interpatch distance Δ_b. Results are based on flow velocities which are computed considering the formulation proposed by *Dronkers* [1964] to model friction.

Figure 8 shows that the approximate solution also describes adequately the influence of the relative interdistance between two patches. Indeed, similar to the experiments described by *Vandenbruwaene et al.* [2011], it is found that when Δ_p increases with respect to the interpatch distance, the flow velocity increases less intensively next to the patches, than in between them.

5. Discussion

5.1. Modeling of Friction

The model introduced here approximates the impact of bottom friction on the flow field by linearizing the friction terms (equations (11) and (12)). In order to quantify the influence of this approximation, we evaluate the governing equations at each order of approximation with a time-stepping procedure (forward Euler) in which the friction terms, occurring in the momentum balance, are described as

$$\gamma \frac{|\boldsymbol{u}|u}{\chi^2 D} = \gamma \frac{\Phi u}{\chi^2 D} \quad \text{and} \quad \gamma \frac{|\boldsymbol{u}|v}{\chi^2 D} = \gamma \frac{\Phi v}{\chi^2 D}, \tag{29}$$

$$\text{with} \quad \Phi = \sqrt{u_{it}^2 + v_{it}^2} \tag{30}$$

where u_{it} and v_{it} are the local flow velocities in the x^* and y^* direction, respectively. The nonlinearity of the bottom friction on the flow field is then accounted for by iterating over the solution, at each time step, until convergence of Φ is obtained.

In Figure 9, a comparison is provided of the velocity normal to the channel obtained considering nonlinear friction, linearizing the friction term and the numerical model. The figure illustrates that the overestimation of the impact of the friction variation is related to the linear treatment of the bottom friction term. In particular, we find that the increase in the amplitude of the flow velocity (next to the patch) is reduced considering nonlinear friction, leading to an increase comparable with that of the numerical model. However, in the regions without significant friction variations, the flow velocities obtained with linear and nonlinear friction are almost identical. Hence, the nonlinearity related to friction exerted at the bottom has a relatively small influence on the flow field on intertidal platforms and a reasonable estimate is found considering linear friction. On the other hand, it must be taken into account that linearizing the bottom friction results in an overestimation of the impact of the spatial variations in friction on the flow velocity.

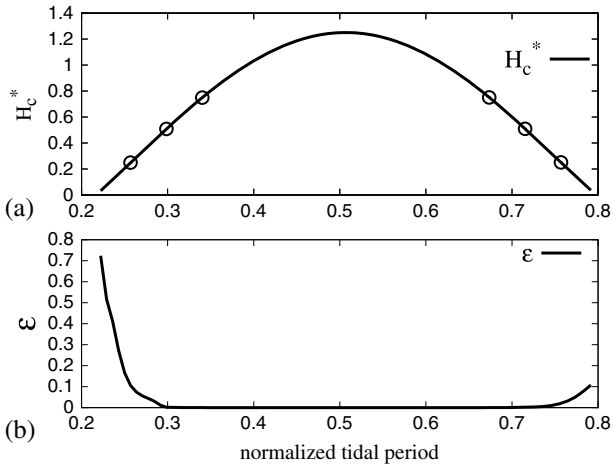

Figure 11. (a) Temporal evolution of the free surface elevation H_c^* in the tidal channel during the inundation phase of the intertidal platform. The circles indicate the timing of the instants plotted in Figures 5 and 6. (b) Corresponding evolution of the parameter ϵ calculated on the basis of results of the complete numerical model.

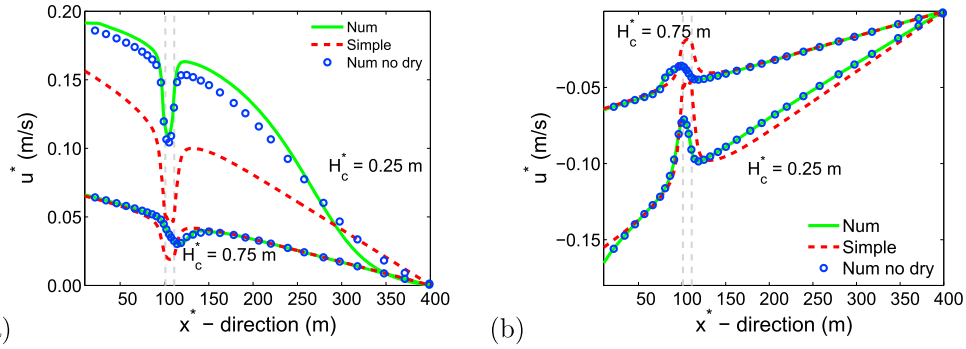

Figure 12. Spatial distribution of the velocity u^* along the transect A-A^0 of Figure 3 during (a) the flood phase and (b) the ebb phase, calculated by the complete numerical model (green line), the approximate model (dashed red line), and the numerical model by limiting the low tide elevation such that the intertidal platform never dries (blue circles). The gray lines indicate the position of the vegetated patch.

Figure 9 also suggests that an improved prediction can be obtained by considering the higher-order formulation of the friction term introduced by *Dronkers* [1964, pp. 296–302] such that

$$u^*|\boldsymbol{u}^*| = (U_0^*)^2\left(\beta u + \mathcal{G}u^3\right), \quad v^*|\boldsymbol{u}^*| = (U_0^*)^2\left(\beta v + \mathcal{G}v^3\right) \tag{31}$$

$$\text{with} \quad \beta = \frac{16}{15\pi} \text{ and } \mathcal{G} = \frac{32}{15\pi}.$$

Adopting this approach, the presented analysis is affected only at order $\mathcal{O}(\epsilon^3)$, leading to additional terms in $K_{3,1}^x$, $K_{3,1}^y$, and $F_{3,1}$. In Appendix 1, the modification to these terms, by considering the formulation proposed by *Dronkers* [1964], is presented. However, the scale-dependent impact of friction variations on the flow, as observed by *Vandenbruwaene et al.* [2011], is not properly represented using *Dronkers*' [1964] treatment of nonlinear friction. This is illustrated in Figure 10, which reports the difference between the flow velocity occurring in between two patches and that next to a patch (observed 30 cm from the patch border and scaled with u_{in}^*) as function of the ratio between the patch dimension and the distance between the two patches. In particular, the flow velocity next to a patch turns out to be larger than that in between two patches for Δ_p/Δ_b larger than 2, which contrasts the laboratory observations. Hence, the adoption of *Dronkers*' [1964] formulation appears less appropriate for the present problem which is characterized by strong gradients in friction; even though for tidal estuaries without variations in friction, the formulation of *Dronkers* [1964] is found to be more accurate than *Lorentz*'s [1926] linearization [see, e.g., *Cai et al.*, 2012].

5.2. Model Capabilities and Limitations

The results presented so far show that the proposed approximate approach provides a computationally stable and robust tool which reasonably describes the flow field on an intertidal platform; also in the

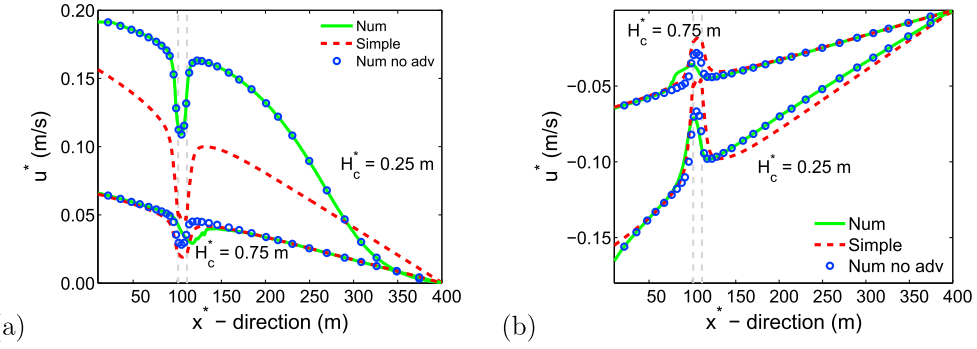

Figure 13. Comparison among the velocity in the x^* direction obtained by the numerical model (green line), the approximate approach (dashed red line), and by neglecting the advective terms in the numerical model (blue circles). The velocity is sampled along the transect A-A^0 of Figure 3 at several instants of the (a) flood and (b) ebb phases. The gray lines indicate the position of the vegetation patch with increased friction.

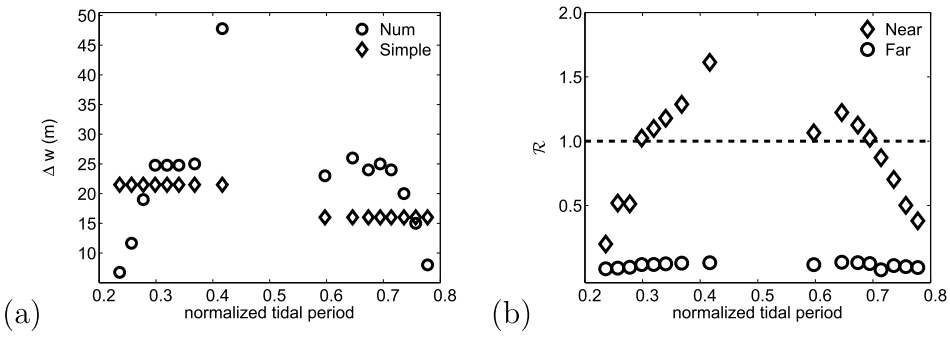

Figure 14. (a) The value of Δw, describing the distance from the patch to the local maxima occurring downstream of the patch, is plotted versus the normalized tidal period during the inundation phase of the intertidal platform. Circles and diamonds refer to values obtained from the numerical model and the approximate solution, respectively. (b) The relative importance $\mathcal{R}$ of the advection terms versus bottom friction, during the inundation phase of the vegetated platform, obtained near the patch (diamonds) and at a farther distance to the patch edge (circles). The magnitude of the friction and advection terms are both calculated on the basis of the results provided by the complete numerical solution.

presence of an heterogeneous distribution of the friction coefficient. Nevertheless, besides the overestimation of the impact of friction variations (related to the linearization of the friction term), some quantitative and qualitative differences are found, which are worthwhile to be discussed. First, Figures 5 and 6 show some discrepancies between the approximate solution and the complete numerical model during the initial flooding phase of the tidal cycle. As briefly mentioned in *Van Oyen et al.* [2012], these differences are related to the features of the tidal wave during the initial flooding of the intertidal platform. In fact, during this phase, larger gradients in the free surface occur such that ϵ is no longer a small parameter and the introduced expansion is, in principle, no longer valid. This aspect is clearly illustrated in Figure 11, reporting the temporal evolution of the elevation of the water surface H_c^* during a tidal cycle and the corresponding value of ϵ:

$$\epsilon = \left[\frac{\varsigma - \varsigma_{av}}{D_{av}}\right]_{av}, \tag{32}$$

where the subscript "av" denotes the average along the transect A-A^0 of Figure 3, evaluated with the values provided by the numerical model.

On the other hand, Figure 12 indicates that the wetting/drying process does not significantly contribute to the difference between the simplified and the numerical model. Indeed, when considering a modified tide in the channel, such that the water level is always larger or equal to 5 cm and, hence, the intertidal platform never dries, the flow velocity in the x^* direction provided by the complete numerical model does not change appreciably. Taken together, Figures 11 and 12 point out that during the initial flooding of the tidal platform, the flow field cannot be described by the sequence of approximate solutions embodied by the linear diffusion equation (23), resulting from the introduced expansion with $\epsilon \ll 1$, such that the solution procedure provides only a limited description of the resulting flow field.

A second limitation of the model, emerging from Figures 5 and 6, consists of the shorter wake at the trailing edge of a vegetated patch predicted by the approximate model. This result essentially depends on the advection of momentum near the friction patches, as shown in Figure 13, reporting the flow velocity in the x^* direction at various instants obtained by the simplified approach, the numerical model and the numerical model in which advection terms are neglected. The figure illustrates that the longer wake at the trailing edge of the vegetated patch is chiefly induced by the advective terms.

The behavior of the wake is further investigated in Figure 14a, showing the temporal distribution, during a tidal cycle, of the distance Δ_w between the edge of a vegetation patch and the downstream local maxima in the flow velocity. It clearly appears that, when using the simplified model, Δ_w keeps nearly constant during the flood and ebb phases (attaining however a lower value in this latter case). Conversely, the complete numerical model indicates that Δ_w first increases during flood, implying thus the formation of a pronounced wake, and then decreases during the ebb phase, especially near the end of the inundation phase.

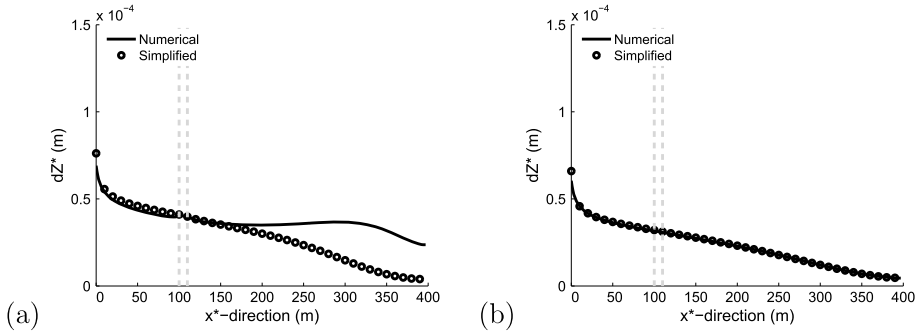

Figure 15. (a) Changes in the bed elevation, dZ^*, occurring after one tidal cycle along the transect A-A^0 (see Figure 3), computed by using the simplified flow field (circles) and the complete numerical model (continuous line). (b) The value of dZ^* after one tidal cycle along the same transect, however, evaluating the erosion, deposition, and suspended sediment concentration only from the instant the normalized tidal period is larger than 0.3, i.e., when the water level in the channel is well above the intertidal platform elevation.

This behavior is rationalized in Figure 14b, where the ratio $\mathcal{R}$ between the magnitude of the advection terms and the magnitude of the bottom friction is plotted for various instants of the tidal cycle when the intertidal platform is inundated. It clearly appears that, close to the patch (diamonds), $\mathcal{R}$ is small during the initial flooding of the intertidal platform and toward the end of the inundation phase, thus inhibiting the elongation of the wake. On the other hand, as high tide is approached, $\mathcal{R}$ attains relatively high values, allowing the elongation of the wake during these phases. This behavior is poorly reproduced by the present model in which the magnitude of the advective terms $\mathcal{O}(\alpha r)$ is assumed to be much smaller than γ and ϵ. This assumption is in any case satisfied far enough from the patch (i.e., at a distance comparable with the patch size) where $\mathcal{R}$ remains small (< 0.1) during the entire inundation period.

5.3. Applicability of the Approach Within a Long-Term Morphological Model

The present approximate solution generally provides an adequate description of the main properties of the flow field, even though minor limitations are apparent, occurring at specific intervals of the tidal cycle, when some of the assumptions at the basis of the analysis are not satisfied. In particular,

1. During the initial flooding phase of the tidal cycle, the approximate solution underestimates (overestimates) the flow velocity near the channel (platform boundary);
2. Near the flow reversal, the approximate solution does not adequately describe the length of the wake at the trailing edge of the vegetated patch.

In order to investigate the implications of these limitations on the application of the approach to evaluate the long-term morphodynamic evolution of salt marshes and tidal flats, we evaluate the changes in the bed elevation after one tidal cycle, resulting from the flow field prescribed by the approximate approach and by the complete continuity and momentum equations. In particular, using the flow field of both approaches, we compute

$$dZ^* = \int_0^{T^*_{m2}} \left[Q^*_d(t') - Q^*_{er}(t') \right] dt', \tag{33}$$

in which T^*_{m2} is the period of a semidiurnal tide, Q^*_d denotes the deposition rate of suspended sediment concentration and Q^*_{er} the erosion rate. The former is regarded to be driven by settling and is estimated by

$$Q^*_d = \begin{cases} w^*_s C \left(1 - \frac{\tau^*_0}{\tau^*_d} \right) & \text{if } \tau^*_0 < \tau^*_d \\ 0 & \text{if } \tau^*_0 \geq \tau^*_d. \end{cases} \tag{34}$$

Here τ^*_d represents a critical shear stress above which sediment no longer settles and is set equal to 0.15 N m^{-2} [*Whitehouse et al.*, 2000; *D'Alpaos et al.*, 2007]; and C denotes the depth-averaged volumetric sediment concentration. In (34), the fall velocity of the suspended sediment is given by w^*_s and is taken to be

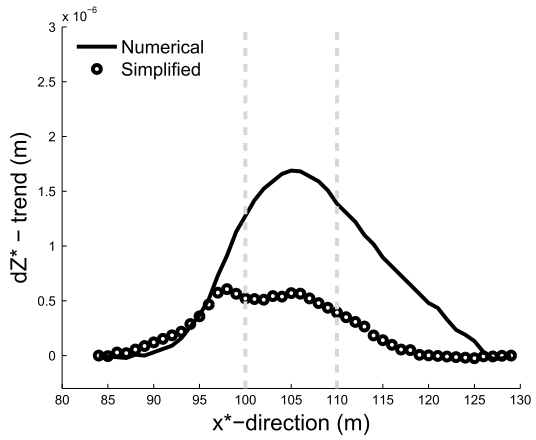

Figure 16. Bed elevation variation along the transect A-A^0 near the friction patch after one tidal cycle. In order to illuminate the variation in the bed elevation increase in and around the patch, the figure plots the value of dZ^* corrected for a linear trend in dZ^* between x^* equal to 84 m and 130 m.

equal to 0.0002 m s^{-1} [*D'Alpaos et al.*, 2007], having assumed a uniform, fine cohesive sediment with grain size equal to 50 μm. Erosion of sediment is described as

$$Q^*_{er} = \begin{cases} Q^*_{e0}\left(\frac{\tau^*_0}{\tau^*_e} - 1\right) & \text{if } \tau^*_0 > \tau^*_e \\ 0 & \text{if } \tau^*_0 \le \tau^*_e, \end{cases} \tag{35}$$

with τ^*_0 the absolute value of the local bottom shear stress, τ^*_e a typical value of shear stress necessary to erode the bed, and Q^*_{e0} an empirical coefficient which depends on the properties of the sediment. In the following, we consider Q^*_{e0} equal to $0.0003/\rho^*_s$ m s^{-1} (ρ^*_s is the sediment density) and τ^*_e = 0.4 N m^{-2} [e.g., *Whitehouse et al.*, 2000; *D'Alpaos et al.*, 2007]. Moreover, the Chézy coefficient, used to evaluate the bottom shear stress, is computed following *van Rijn* [1984a]. In (33), sediment trapping related to the presence of vegetation is not considered, in order to focus on the impact of the flow field on the sediment dynamics.

The temporal evolution and spatial distribution of the suspended sediment concentration on the intertidal platform is described by solving the classical two-dimensional advection-diffusion equation

$$\frac{\partial D^*C}{\partial t^*} + \frac{\partial u^*D^*C}{\partial x^*} + \frac{\partial v^*D^*C}{\partial y^*} = k^*_m\left[\frac{\partial}{\partial x^*}\left(D^*\frac{\partial C}{\partial x^*}\right) + \frac{\partial}{\partial y^*}\left(D^*\frac{\partial C}{\partial y^*}\right)\right] + Q^*_{er} - Q^*_d, \tag{36}$$

for the sediment concentration $C(x^*, t^*)$. In (36), k^*_m denotes the horizontal mixing coefficient, which is considered constant and equal to 0.3 m^2 s^{-1} for simplicity, see *D'Alpaos et al.* [2007, and references therein].

At the channel boundary, we impose a constant concentration during the entire cycle (C^*_{ext} = 0.05 g/l), while a vanishing sediment flux (i.e., a zero concentration gradient) is assumed at the boundary of the intertidal platform. Initially, the suspended sediment concentration on the platform is set to zero.

Figure 15a reports the value of dZ^* on the intertidal platform along the transect A-A^0 (see Figure 3 of the manuscript), computed with the flow field obtained by the numerical model and the approximate approach; respectively full line and circles. The values of dZ^* obtained with both models are almost equal close to the channel, the changes in the bed being slightly larger when considering the simplified method. Conversely, the simplified model tends to underestimate bed accretion near the divide of the intertidal platform, where a vanishing sediment flux condition has been imposed.

On the other hand, if we rule out the effects of the initial flooding phase, e.g., start the simulation at the instant the normalized tidal period is equal to 0.3, the two models display an almost perfect agreement (Figure 15b). In Figure 15b, we consider as initial condition the suspended sediment concentration to decrease linearly in the x^* direction from the channel boundary toward the end of the intertidal platform. Similar results are obtained when starting from a spatially uniform suspended sediment concentration (not shown).

The discrepancies obtained in Figure 15a are thus related to the lower flow velocities provided by the approximate approach when the intertidal platform begins to be flooded. In particular, due to the higher flow velocities predicted by the numerical model, the suspended sediment is more effectively advected toward the end of the intertidal platform, leading to higher sediment concentration and thus an increase in the deposition. In addition, the higher flow velocities inhibit the deposition of the sediment near the channel, due to settling lag effects (here modeled by introducing τ_d) leading to the small difference in dZ^* near the channel. On the other hand, Figure 15b also indicates that the discrepancies in the flow velocity at the trailing edge of the vegetated patches, occurring near flow reversal, do not introduce significant differences in the changes in the bed elevation.

Finally, as illustrated by Figure 16, which provides a detailed picture on the changes in the bed near the patch, the impact of the variation in friction is also reasonably well reproduced in the vicinity of the vegetation patch. Figure 16 plots the value of dZ^* corrected for a linear trend in dZ^* between x^* equal to 84 m and x^* equal to 130 m (in order to facilitate the illustration of the impact of the friction patch). Even though the increase in bed elevation is less pronounced for the simplified model, the figure shows that both models lead to an additional accretion of sediment before, within, and after the patch and thus describe a similar trend.

It can then be concluded that applying the approximate solution within a morphodynamic model will provide a reasonable estimate of the morphodynamic evolution of the bed; however, it should be kept in mind that the approach will result in an underestimate of the increase in bottom elevation near the end of the platform.

On the other hand, the present approach has the advantage that the computational effort required by the simplified model is significantly smaller than that to solve numerically the complete governing equations. It is not straightforward to quantify this advantage, since different numerical models adopt distinct time-stepping approaches, spatial discretization methods, etc. However, many numerical approaches use the (semi)implicit method introduced by *Casulli and Cheng* [1992] [see *Vitousek and Fringer*, 2013, and references therein], which removes the restriction on the time step due to the Courant-Friedrichs-Lewy (CFL)-criterium, related to the propagation of the free surface elevation. Considering a finite difference discretization, this approach leads to a system of equations which is similar to that described in (28). In particular, discretization of spatial derivatives leads for both approaches to a five-diagonal unsymmetric matrix. Hence, each time the system of equations is solved, approximately similar computation time is required.

The advantage of the introduced expansion is that the procedure leads to a set of linear equations, i.e., the relations described by equation (23). This facilitates the use of Fourier series to obtain the solution of the flow field elevation during the tidal cycle. As such, the solution of the algebraic system resulting from the discretization of the spatial derivatives appearing in (28), and involving the five-diagonal unsymmetric matrix mentioned above, only needs to be evaluated N times. In the presented results, 35 harmonics are considered (i.e., $N = 35$).

Conversely, with a numerical approach, the system of equations, resulting from the spatial discretization of the governing equations, is solved each time step. Hence, the computational advantage following from the approximate solution can be estimated by evaluating the ratio between the number of the time steps necessary to compute one tidal cycle with a numerical model N_{num}, and the number of harmonics considered in the Fourier series N. The former is dictated to be the maximum time step Δt^*_{max} allowed. In particular, considering the procedure introduced by *Casulli and Cheng* [1992], the maximum time step is still restricted due to the CFL-criterium induced by the advective terms in the momentum balance. Taking into account that we want to solve the impact on friction of vegetation patches with small spatial scales (i.e., $\mathcal{O}(5)$ m, see Figure 1), it is necessary to consider relatively small grid sizes and, as a consequence, restrictively small Δt^*_{max}. For example, considering the horizontal grid spacing Δx equal to 0.2 m, with a characteristic velocity of 0.1 m s^{-1} reveals that $\Delta t^*_{max} \sim \mathcal{O}(1)$ s. Hence, considering a tidal wave which floods the intertidal platform during half of the tidal period, $N_{num} \approx 20,000$. Following this reasoning, we can estimate that the introduced approach is approximately $N_{num}/N \sim \mathcal{O}(500)$ times more economic than standard numerical procedures.

On the other hand, as illustrated by Figure 15b and discussed above, it is possible to neglect advection of momentum without any significant consequences to the description of the suspended sediment concentration. This suggests that, with the objective to study the morphodynamic development of the intertidal platform, also numerical models could obtain a significant speed up by neglecting the advection terms, allowing larger time steps (i.e., $\Delta t^*_{max} \sim \mathcal{O}(50)$ s). Nevertheless, even considering Δt^*_{max} equal to 50 s, the introduced procedure turns out to be approximately 10 times more economic. Hence, it appears that the approximate approach provides a significantly more economic solution, while still ensures a reasonable level of accuracy, as far as the distribution of the changes in the bed elevation is concerned.

Taken together the limitations discussed above and the computational advantages just considered, we deem that the proposed procedure provides a valuable simplified hydrodynamical tool to investigate efficiently the long-term morphodynamic evolution of a vegetated intertidal platform; especially when

exploring the relevant parameter space (e.g., tidal range, sediment features, and vegetation characteristics) in order to unravel the governing processes controlling the evolution of tidal environments such as salt marshes and mangrove forests.

5.4. Comparison With the Approach of *Friedrichs and Madsen* [1992]

In order to complete the investigation of the performance of the present approach, a comparison of the obtained results with the flow field acquired by considering the approach introduced by *Friedrichs and Madsen* [1992] is performed. At the first order of approximation, this procedure leads to a similar set of governing equations as obtained in the present model, see Appendix B equation (B8). This can be expected since the expansion performed by *Friedrichs and Madsen* [1992] is similar to the one described in the present manuscript. However, at the following order of approximation, the approach described by *Friedrichs and Madsen* [1992] and the present model has an essential difference. In particular, the former suggests to employ the solution obtained at the leading order of approximation to describe the time variation of the relevant parameters at the following order of approximation. As described in detail in Appendix B, this approach leads to flow velocities which are opposite to those predicted by the other two models, during the phases of the tidal cycle where the water on the intertidal platform becomes shallow (i.e., when $H_c^* < 0.3$). As such, it can be concluded that *Friedrichs and Madsen*'s [1992] approach is not suitable to describe the flow field on a vegetated intertidal platform for large time intervals of the tidal cycle.

6. Conclusions

Overall, the approximate solution suggested in the present study is found to provide a reliable qualitative and quantitative description of the tidal flow field over an intertidal platform. In particular, the model fairly reproduces the flow velocities on the platform in comparison with the numerical model of *Carniello et al.* [2011], capturing the local reduction and amplification of the flow field, within and next to a vegetation patch, respectively. In fact, it is found that the model (qualitatively) correctly describes the scale-dependent impact of friction patches on the flow field, as revealed by laboratory experiments [*Vandenbruwaene et al.*, 2011].

A number of limitations related to the approach are however present. First, the simplified procedure overestimates the reduction (amplification) of the magnitude of the flow velocity within (next to) the friction patches. It is demonstrated that this derives from the linearization of the friction term in the momentum balance. On the other hand, in the portions of the domain where strong friction variations are absent, linear friction does not significantly affect the resulting flow velocity. Hence, on intertidal platforms, the nonlinearity related to bottom friction has a relative small impact on the flow field. In addition, it is found that the approach suggested by *Dronkers* [1964] reduces the discrepancy related to the linearization of the friction term, but it does not capture the scale-dependent effect of friction patches on the flow velocity. It follows that *Dronkers*' [1964] approach is less appropriate for the problem under consideration.

Next, near tidal reversal, the approximate solution predicts a shorter wake at the lee side of the vegetation patches. Analyzing the relative contribution of the advection and bottom friction term in the momentum balance, we find that this variation can be ascribed to the negligence of advection terms in the approximate procedure. In fact, when considering the numerical solution, near the patches (characterized by strong gradients of the friction), the magnitude of the advection of momentum is found to be larger than the magnitude of the bottom friction, close to high tide. Hence, during these phases, the assumption $\alpha \ll \gamma$, at the basis of the expansion used to derive the simplified solution, does not hold, limiting its performance.

Finally, at the initial flooding phase of the tidal cycle, the approximate solution underestimates the flow velocities near the channel and provides larger values of the velocity near the watershed divide. This discrepancy is found to be induced by the strong gradients in the free surface elevation occurring during this phase of the tide on the platform. These stronger gradients lead to large values of ϵ which inhibit the correct description of the problem by means of a sequence of linear diffusion equations as obtained using the approximate procedure.

Evaluating the bed evolution on the intertidal platform after one tidal cycle based on the flow velocity computed with the simplified approach and the numerical model, the first two limitations, however, are found to have negligible impact on the sediment dynamics. The latter, on the other hand, induces that the changes in the bed elevation, near the boundaries of the intertidal platform, are smaller based on the approxi-

mate approach than when the numerical model is considered to compute dZ^*. Within and in the vicinity of the friction patches, however, similar trends of additional accumulation of sediment are found with both models.

Hence, within a morphodynamic model, the approximate solution will result in reasonable estimates of the evolution of the bed elevation. Taking into account, in addition, that the approach is significantly ($\sim \mathcal{O}(100)$ times) computationally more efficient than a full-fledged numerical model, we conclude that the proposed approach provides a suitable method to evaluate the interaction between inhomogeneous vegetation cover, topography, and the tidal flow field within the aim to investigate to the long-term morphodynamic evolution of tidal wetlands.

Appendix A: Solution Considering Friction as Proposed by *Dronkers* [1964]

Assuming the higher-order formulation of the friction term introduced by [*Dronkers*, 1964], the known terms in the approximate relations obtained from the momentum balance and the forcing term appearing in the mass balance, at the third order of approximation, change. The resulting equations are then given by

$$\left(K^x_{3,1}\right)^D = \frac{u_{21}D_{11}}{D_0} + \frac{u_{11}D_{21}}{D_0} - \frac{u_{11}D_{11}^2}{D_0^2} - \frac{\mathcal{G}}{\beta}u_{11}^3, \tag{A1}$$

$$\left(K^y_{3,1}\right)^D = \frac{v_{21}D_{11}}{D_0} + \frac{v_{11}D_{21}}{D_0} - \frac{v_{11}D_{11}^2}{D_0^2} - \frac{\mathcal{G}}{\beta}v_{11}^3. \tag{A2}$$

$$\begin{aligned}(F_{3,1})^D = r\Bigg[&\frac{\partial}{\partial x}\left(2u_{21}D_{11} + 2u_{11}D_{21} - \frac{u_{11}D_{11}^2}{D_0} - \frac{D_0\mathcal{G}u_{11}^3}{\beta}\right)\\ &+ \frac{\partial}{\partial y}\left(2v_{21}D_{11} + 2v_{11}D_{21} - \frac{v_{11}D_{11}^2}{D_0} - \frac{D_0\mathcal{G}v_{11}^3}{\beta}\right)\Bigg],\end{aligned} \tag{A3}$$

where the superscript D denotes that the formulation proposed by *Dronkers* [1964] is considered.

Appendix B: Solution Following the Approach Presented by *Friedrichs and Madsen* [1992]

Contrary to the presented approach, *Friedrichs and Madsen* [1992] do not split the free surface elevation into a spatially averaged part $\xi(t)$ and the variation of the free surface $\zeta(x, y, t)$ with respect to ξ. Considering the nondimensional variables introduced in (4) and (5), the governing equations are then given by

$$\alpha\left\{\frac{\partial u}{\partial t} + r\left(u\frac{\partial u}{\partial x} + v\frac{\partial u}{\partial y}\right)\right\} = -\frac{\partial H}{\partial x} - \gamma\frac{\lambda u}{\chi^2 D}, \tag{B1}$$

$$\alpha\left\{\frac{\partial v}{\partial t} + r\left(u\frac{\partial v}{\partial x} + v\frac{\partial v}{\partial y}\right)\right\} = -\frac{\partial H}{\partial y} - \gamma\frac{\lambda v}{\chi^2 D}, \tag{B2}$$

$$\frac{\partial H}{\partial t} + r\left\{\frac{\partial}{\partial x}(Du) + \frac{\partial}{\partial y}(Dv)\right\} = 0, \tag{B3}$$

where friction is linearized considering equations (11) and (12) to simplify the comparison. However, as discussed in section 5, this procedure does not significantly affect the results.

In the first step, *Friedrichs and Madsen* [1992] consider that frictional effects are much larger than acceleration, which corresponds to the assumption that $\alpha \ll 1$. It follows that

$$u = -\frac{\chi^2 D}{\gamma\lambda}\frac{\partial H}{\partial x} \quad \text{and} \quad v = -\frac{\chi^2 D}{\gamma\lambda}\frac{\partial H}{\partial y}. \tag{B4}$$

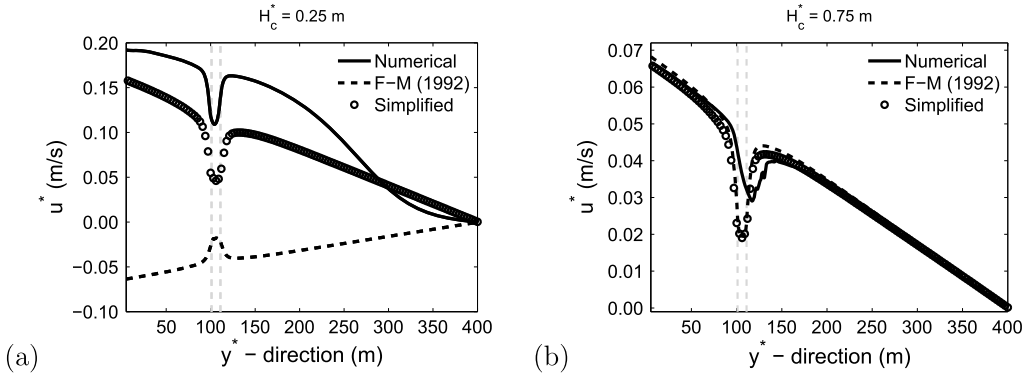

Figure B1. Comparison of the value of u^* along the transect A-A^0 depicted in Figure 3, obtained by the introduced procedure (circles), the approach suggested by *Friedrichs and Madsen* [1992] (dashed lines), and the full-fledged numerical model (full lines). The flow velocities in the x^* direction are depicted for the instants H_c^* equals 0.25 and 0.75 m in Figures B1a and B1b, respectively.

Substitution of (B4) into (B3) leads to

$$\frac{\partial H}{\partial t} - r\left\{\frac{\partial}{\partial x}\left(\frac{D^2\chi^2}{\lambda\gamma}\frac{\partial H}{\partial x}\right) + \frac{\partial}{\partial y}\left(\frac{D^2\chi^2}{\lambda\gamma}\frac{\partial H}{\partial y}\right)\right\} = 0. \tag{B5}$$

Subsequently, *Friedrichs and Madsen* [1992] consider an expansion in the variables which contribute to the time variability of the diffusion coefficient, assuming that the variation in time of the relevant parameters is small with respect to their time-averaged value. Thus, regarding (B5), this implies that the local depth D is given by

$$D = D_0^\dagger(x,y) + D_1^\dagger(x,y,t) \text{ with } D_1^\dagger \ll D_0^\dagger. \tag{B6}$$

Here $D_0^\dagger(x,y)$ denotes the time-averaged depth and $D_1^\dagger(x,y,t)$ the variation of D with respect to $D_0^\dagger$. Moreover, considering $D_1^\dagger$ much smaller than $D_0^\dagger$, it follows that

$$D^2 \approx (D_0^\dagger)^2 + 2D_0^\dagger D_1^\dagger. \tag{B7}$$

Note that the expansion introduced by *Friedrichs and Madsen* [1992] (B6) differs from the presently considered expansion (14), since (B6) considers the variation of the free surface to be small with respect to the time-averaged free surface elevation, while (14) regards the difference between the free surface elevation and its spatially averaged value to be small.

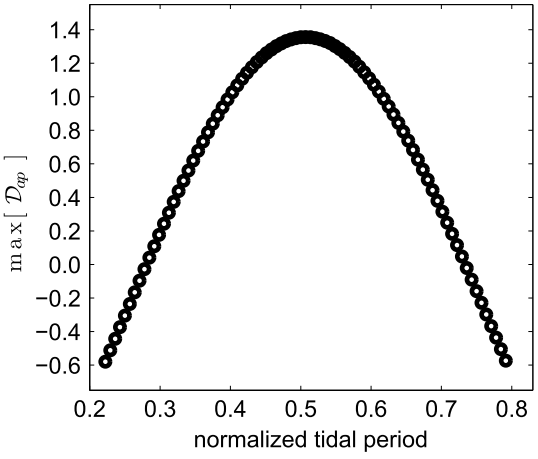

Figure B2. Maximum value of $\mathcal{D}_{ap}$ occurring on the intertidal platform plotted versus the normalized tidal period.

At leading order of approximation, we retain from equation (B5),

$$\frac{\partial H}{\partial t} - r\left\{\frac{\partial}{\partial x}\left(\frac{(D_0^\dagger)^2\chi^2}{\lambda\gamma}\frac{\partial H}{\partial x}\right) + \frac{\partial}{\partial y}\left(\frac{(D_0^\dagger)^2\chi^2}{\lambda\gamma}\frac{\partial H}{\partial y}\right)\right\} = 0. \tag{B8}$$

which, in fact, is identical to equation (20).

Since, we aim to consider generic bed elevations and friction characteristics, we do not make any further approximation on $D_0^\dagger$ and χ in order to solve (B8) as proposed by *Friedrichs*

and Madsen [1992]. However, equation (B8) is solved by means of a time-stepping procedure (forward Euler) with a finite difference scheme, to obtain a solution of $H(x, t)$.

In the third step, *Friedrichs and Madsen* [1992] use the solution obtained at the leading order of approximation to estimate the time variability of the diffusion coefficient. This means that the values of H, found at the leading order of approximation, are used to describe $D_1^\dagger(t)$ and equation (B5) is approximated as

$$\frac{\partial H}{\partial t} - r\left\{\frac{\partial}{\partial x}\left(\frac{[(D_0^\dagger)^2 + 2D_0^\dagger D_1^\dagger]\chi^2}{\lambda\gamma}\frac{\partial H}{\partial x}\right) + \frac{\partial}{\partial y}\left(\frac{[(D_0^\dagger)^2 + 2D_0^\dagger D_1^\dagger]\chi^2}{\lambda\gamma}\frac{\partial H}{\partial y}\right)\right\} = 0. \tag{B9}$$

Since we evaluate (B9) by means of a numerical finite difference scheme, we relax the assumption made by *Friedrichs and Madsen* [1992] in which $D_1^\dagger(x, y, t)$ at a certain point is chosen representative for the entire domain and allow $D_1^\dagger(x, y, t)$ to vary also spatially. Solving (B9), we obtain $H(x, y, t)$ which then can be used to compute the flow velocity, reminding that

$$u = -\frac{\chi^2 D}{\gamma\lambda}\frac{\partial H}{\partial x} \quad \text{and} \quad v = -\frac{\chi^2 D}{\gamma\lambda}\frac{\partial H}{\partial y}. \tag{B10}$$

Figure B1 shows the spatial distribution, along the transect A-A^0 of Figure 3, of the flow velocity in the x^* direction computed by using the present model, *Friedrichs and Madsen*'s [1992] approach, and the full-fledged numerical model. Two instants of the flooding phase of the tidal cycle (H_c^* equal to 0.25 m and 0.75 m, Figures B1a and B1b, respectively) are considered. Near the tidal reversal (H_c^* equal to 0.75 m), the approach of *Friedrichs and Madsen* [1992] and the present one provide similar results, both reproducing reasonably the complete numerical solution. However, at the beginning of the flooding phase, the approach of *Friedrichs and Madsen* [1992] leads to flow velocities which are opposite to those predicted by the other two models. Similar results are obtained during the ebb phase (not shown here).

This result, characterizing the phases of the tidal cycle, where the water depth on the intertidal platform becomes shallow (i.e., $H_c^* < 0.3$), arises directly from the approximation of the time variation of the diffusion coefficient in the final governing equations, estimated through the solution obtained at the leading order of approximation. Indeed, *Friedrichs and Madsen* [1992] consider $D_1^\dagger \ll D_0^\dagger$ such that the approximate diffusion coefficient in equation (B9), governing the free surface elevation, is given by $\mathcal{D}_{ap} = (D_0^\dagger)^2 + 2D_0^\dagger D_1^\dagger$. However, in shallow environments (such as on an intertidal platform), the assumption that the time variation of the local depth is much smaller than its time-average is not valid. In other words, $\mathcal{D}_{ap}$ is only a crude approximation of D^2 for the problem under consideration, which leads to the unphysical results depicted in Figure B1. Indeed, Figure B2 indicates that the maximum value of $\mathcal{D}_{ap}$ (occurring in the domain) attains negative values for the phases of the tidal cycle characterized by a small depth. Hence, for these phases, the free surface elevation H is oppositely diffused by (B9) and the spatial gradient of H is reversed, thus leading to the reversed flow velocity shown in Figure B1a. Hence, it can be concluded that *Friedrichs and Madsen*'s [1992] approach provides an incorrect description of the flow field on a vegetated intertidal platform for large time intervals of the tidal cycle. Moreover, the analysis described above demonstrates that this is a direct result of the use of the values obtained at the leading order of approximation to describe the time variation of the diffusion coefficient at the subsequent order of approximation.

Acknowledgments
The first author wishes to acknowledge Ghent University (Special Research Fund) for his postdoctoral grant. The research has been partially stimulated by the Scientific Research Community: "The functioning of river ecosystems through plant-flow-soil interactions" funded by FWO (Research Foundation Flanders). Partial funding has been provided by the University of Padua, within the projects "Morphodynamics of marsh systems subject to natural forcings and climate changes" and "Combined use of remote sensing and in situ measurements for the calibration of transport and diffusion models in shallow coastal lagoons". A.D. gratefully acknowledges the Fondazione Caiparo Project: "Reading signatures of the past to predict the future— PASTtoFUTURE". The authors wish to thank one anonymous reviewer and Marco Toffolon for their thorough review which has helped to improve the manuscript substantially.

References

Allen, J. (1990), Salt-marsh growth and stratification: A numerical model with special reference to the Severn Estuary, Southwest Britain, *Mar. Geol.*, *95*, 77–96.

Balke, T., P. Klaassen, A. Garbutt, D. van der Wal, P. Herman, and T. Bouma (2012), Conditional outcome of ecosystem engineering: A case study on tussocks of the salt marsh pioneer Spartina anglica, *Geomorphology*, *153–154*, 232–238, doi:10.1016/j.geomorph.2012.03.002.

Bollhoefer, M., and Y. Saad (2006), Multilevel preconditioners constructed from inverse-based ILUS, *SIAM J. Sci. Comput.*, *27*, 1627–1650.

Cai, H., H. H. G. Savenije, and M. Toffolon (2012), A new analytical framework for assessing the effect of sea-level rise and dredging on tidal damping in estuaries, *J. Geophys. Res.*, *117*, C09023, doi:10.1029/2012JC008000.

Carniello, L., A. Defina, S. Fagherazzi, and L. D'Alpaos (2005), A combined wind wave-tidal model for the Venice lagoon, Italy, *J. Geophys. Res.*, *110*, F04007, doi:10.1029/2004JF000232.

Carniello, L., A. D'Alpaos, and A. Defina (2011), Modeling wind waves and tidal flows in shallow micro-tidal basins, *Estuarine Coastal Shelf Sci.*, *92*, 263–276, doi:10.1016/j.ecss.2011.01.001.

Casulli, V., and R. Cheng (1992), Semi-implicit finite difference methods for three-dimensional shallow water flow, *Int. J. Numer. Methods Fluids*, *15*, 629–648.

Costanza, R., et al. (1997), The value of the world's ecosystem services and natural capital, *Nature*, *387*, 252–260.

D'Alpaos, A. (2011), The mutual influence of biotic and abiotic components on the long-term ecomorphodynamic evolution of salt-marsh ecosystems, *Geomorphology*, *126*, 269–278, doi:10.1016/j.geomorph.2010.04.027.
D'Alpaos, A., S. Lanzoni, M. Marani, S. Fagherazzi, and A. Rinaldo (2005), Tidal network ontogeny: Channel initiation and early development, *J. Geophys. Res.*, *110*, F02001, doi:10.1029/2004JF000182.
D'Alpaos, A., S. Lanzoni, M. Marani, and A. Rinaldo (2007), Landscape evolution in tidal embayments: Modeling the interplay of erosion, sedimentation and vegetation dynamics, *J. Geophys. Res.*, *112*, F01008, doi:10.1029/2007JF000537.
D'Alpaos, A., S. M. Mudd, and L. Carniello (2011), Dynamic response of marshes to perturbations in suspended sediment concentrations and rates of relative sea level rise, *J. Geophys. Res.*, *116*(F4), F04020, doi:10.1029/2011JF002093.
Day, J., L. D. Britsch, S. Hawes, G. Shaffer, D. Reed, and D. Cahoon (2000), Pattern and process of land loss in the Mississippi Delta: A spatial and temporal analysis of wetland habitat change, *Estuaries*, *23*, 425–438.
Defina, A. (2000), Two-dimensional shallow flow equations for partially dry areas, *Water Resour. Res.*, *36*(11), 3251–3264.
Dronkers, J. (1964), *Tidal Computations in Rivers and Coastal Waters*, North-Holland, Amsterdam.
Fagherazzi, S., et al. (2012), Numerical models of salt marsh evolution: Ecological, geomorphic, and climatic factors, *Rev. Geophys.*, *50*, RG1002, doi:10.1029/2011RG000359.
French, J. (1993), Numerical simulation of vertical marsh growth and adjustment to accelerated sea-level rise, North Norfolk, U. K., *Earth Surf. Processes Landforms*, *18*, 63–81.
Friedrichs, C., and O. Madsen (1992), Nonlinear diffusion of the tidal signal in frictionally dominated embayments, *J. Geophys. Res.*, *97*, 5637–5650.
Kirwan, M., and A. Murray (2007), A coupled geomorphic and ecological model of tidal marsh evolution, *Proc. Natl. Acad. Sci. U.S.A*, *104*, 6118–6122, doi:10.1073/pnas.0700958104.
LeBlond, P. (1978), On tidal propagation in shallow rivers, *J. Geophys. Res.*, *83*, 4717–4721.
Lorentz, H. (1926), Verslag Staatcommissie Zuiderzee 1918–1926, *Tech. Rep.*, Rep. Govt. Zuiderzee Comm, Alg. Landsddrukkerij, Den Haag.
Marani, M., E. Belluco, A. D'Alpaos, A. Defina, S. Lanzoni, and A. Rinaldo (2003), On the drainage density of tidal networks, *Water Resour. Res.*, *39*(2), 1040, doi:10.1029/2001WR001051.
Mitsch, W. (2000), *Wetlands*, Wiley, New York.
Morris, J., P. Sundareshwar, C. Nietch, B. Kjerfve, and D. Cahoon (2002), Responses of coastal wetlands to rising sea level, *Ecology*, *83*, 2869–2877.
Rinaldo, A., S. Fagherazzi, S. Lanzoni, M. Marani, and W. Dietrich (1999), Tidal networks: 2. Watershed delineation and comparative network morphology, *Water Resour. Res.*, *12*, 3905–3917.
Schuttelaars, H., and H. de Swart (1999), Initial formation of channels and shoals in short tidal embayments, *J. Fluid Mech.*, *386*, 15–42.
Tambroni, N., and G. Seminara (2012), A one-dimensional eco-geomorphic model of marsh response to sea level rise: Wind effects, dynamics of the marsh border and equilibrium, *J. Geophys. Res.*, *117*, F03026, doi:10.1029/2012JF002363.
Temmerman, S., T. Bouma, J. Van der Koppel, D. Van der Wal, M. De Vries, and P. Herman (2007), Vegetation causes channel erosion in a tidal landscape, *Geology*, *35*(7), 631–634.
Toffolon, M., and S. Lanzoni (2010), Morphological equilibrium of short channels dissecting the tidal flats of coastal lagoons, *J. Geophys. Res.*, *115*, F04036, doi:10.1029/2010JF001673.
Vandenbruwaene, W., et al. (2011), Flow interaction with dynamic vegetation patches: Implications for biogeomorphic evolution of a tidal landscape, *J. Geophys. Res.*, *116*, F01008, doi:10.1029/2010JF001788.
Vitousek, S., and O. Fringer (2013), Stability and consistency of non-hydrostatic free-surface models using the semi-implicit θ-method, *Int. J. Numer. Methods Fluids*, *72*, 550–582.
Van Oyen, T., S. Lanzoni, A. DAlpaos, S. Temmerman, P. Troch, and L. Carniello (2012), A simplified model for frictionally dominated tidal flows, *Geophys. Res. Lett.*, *39*, L12403, doi:10.1029/2012GL051949.
van Rijn, L. C. (1984a), Sediment transport, Part 1: Bed load transport, *J. Hydraul. Eng.*, *110*, 1431–1456.
van Rijn, L. C. (1984b), Sediment transport, Part 2: Suspended load transport, *J. Hydraul. Eng.*, *110*, 1613–1641.
Whitehouse, R., R. Soulsby, W. Roberts, and H. Mitchener (2000), *Dynamics of estuarine muds*, Thomas Telford, Heron Quay, London.
Zong, L., and H. Nepf (2010), Flow and deposition in and around a finite patch of vegetation, *Geomorphology*, *116*, 363–372.